

From Methane to Methanol: Pd-iC-CeO₂ Catalysts Engineered for High Selectivity via Mechanochemical Synthesis

Juan D. Jiménez, Pablo G. Lustemberg,* Maila Danielis, Estefanía Fernández-Villanueva, Sooyeon Hwang, Iradwikanari Waluyo, Adrian Hunt, Dominik Wierzbicki, Jie Zhang, Long Qi, Alessandro Trovarelli, José A. Rodriguez, Sara Colussi, M. Verónica Ganduglia-Pirovano,* and Sanjaya D. Senanayake*

Cite This: *J. Am. Chem. Soc.* 2024, 146, 25986–25999

Read Online

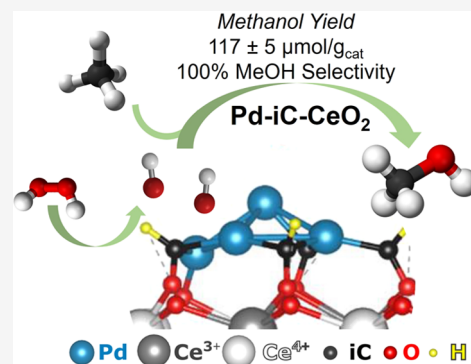
ACCESS |

Metrics & More

Article Recommendations

Supporting Information

ABSTRACT: In the pursuit of selective conversion of methane directly to methanol in the liquid-phase, a common challenge is the concurrent formation of undesirable liquid oxygenates or combustion byproducts. However, we demonstrate that monometallic Pd-CeO₂ catalysts, modified by carbon, created by a simple mechanochemical synthesis method exhibit 100% selectivity toward methanol at 75 °C, using hydrogen peroxide as oxidizing agent. The solvent free synthesis yields a distinctive Pd-iC-CeO₂ interface, where interfacial carbon (iC) modulates metal-oxide interactions and facilitates tandem methane activation and peroxide decomposition, thus resulting in an exclusive methanol selectivity of 100% with a yield of 117 μmol/g_{cat} at 75 °C. Notably, solvent interactions of H₂O₂ (aq) were found to be critical for methanol selectivity through a density functional theory (DFT)-simulated Eley–Rideal-like mechanism. This mechanism uniquely enables the direct conversion of methane into methanol via a solid–liquid–gas process.



INTRODUCTION

The direct utilization of natural gas, which is primarily composed of methane (CH₄) and is a potent greenhouse gas, presents a significant scientific challenge.¹ This challenge is mainly attributed to the strong C–H bonds of methane (104 kcal/mol), which tend to drive methane to overoxidation into undesirable CO₂ rather than useful chemicals. The direct conversion of natural gas into liquid fuels, such as methanol (CH₃OH), through a single-step process, is an attractive option. This method offers several advantages, including the ease of transporting liquid oxygenates compared to pressurized or liquified gases from highly localized and remote natural gas well locations. Biomimetic approaches that mimic nature’s own methane monooxygenase enzymes, typically employing zeolites, often face limitations such as high temperature requirements, which lead to selectivity toward undesirable combustion products.² In contrast, heterogeneous catalysts based on metal oxides have shown promise in directing selectivity toward methanol using various active materials like Rh/ZrO₂,³ Pd/TiO₂,⁴ Ni/CeO₂,⁵ CeO₂/CuO/Cu(111),⁶ Ir-based systems^{7,8} and FeO_x/TiO₂.⁹ They offer advantages like a high dispersion of the active metal sites and facilitate intimate contact between the reducible support and metal sites.¹⁰

Gas phase conversion of methane to methanol generally consist of sequentially cycled O₂ activation, CH₄ reaction, and a final H₂O purge step,¹¹ each at distinctly different operating conditions, while liquid phase methane to methanol is

facilitated by being a one pot synthesis at a fixed condition in either H₂O₂ (aq)¹² or an O₂/H₂O environment.⁸ Studies aimed at elucidating the reaction mechanism of direct methane to methanol (MtM) conversion in the presence of gas-phase H₂O₂ or O₂ using metal/oxide catalysts have made significant progress.³ These studies have identified AuPd active sites capable of generating peroxide in situ,^{13,14} explore the influence of oxidants and CO on reaction intermediates, and revealed distinct mechanisms when using H₂O₂ as an oxidant^{8,15} versus molecular oxygen.¹⁶ With peroxide, it is generally accepted that two independent catalytic cycles occur. The first involves the decomposition of hydrogen peroxide, resulting in the formation of 2OH* species. Simultaneously, methane is converted into methyl, CH₃, which undergoes sequential oxidation to methanol and eventually CO₂ as the final product at higher temperatures and longer reaction times.¹⁷ A similar stepwise conversion could take place in the liquid phase for the MtM process on Cu₁–Ag₁/ZSM-5 catalysts.^{18,19} However, in the case of liquid phase batch

Received: April 9, 2024
Revised: August 2, 2024
Accepted: August 6, 2024
Published: August 15, 2024



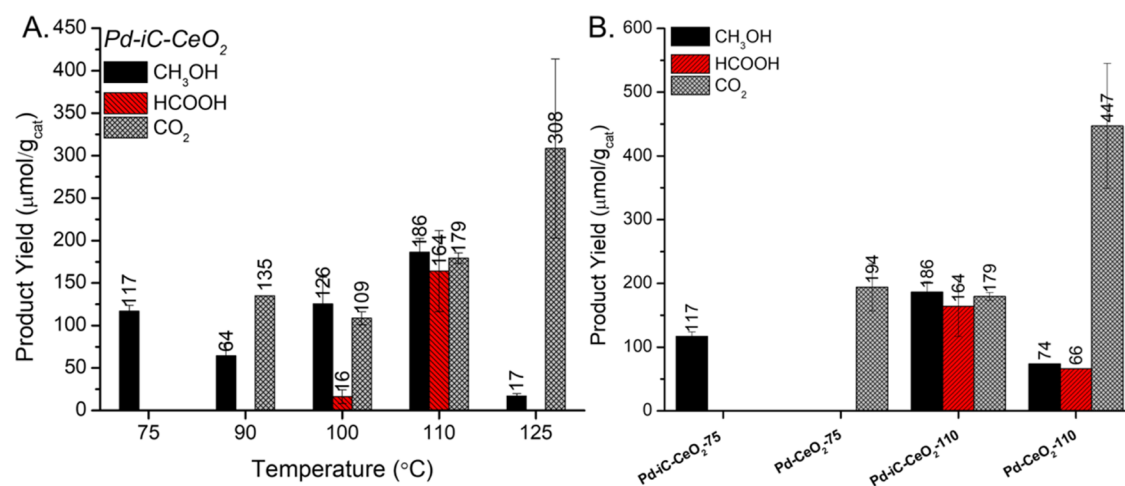


Figure 1. Reactivity of Pd-CeO₂ materials for direct methane to methanol conversion in a batch mode reactor. (A) Methanol, HCOOH and CO₂ yield as a function of temperature (75–125 °C) for Pd-iC-CeO₂, (B) comparison between reference materials at 75 or 110 °C. Reaction conditions: 25 mg of catalyst, 1 h reaction time, 15 mL of 0.5 M H₂O₂ (aq), 20 bar initial pressure of 20% CH₄ in Ar balance, 800 rpm mixing.

mode reactions, the precise mechanism of methane to methanol remains elusive due to the challenge of characterizing the catalyst and reaction intermediates in the liquid phase. Furthermore, the possible existence of a metal–carbon-oxide interface could affect the selectivity for methanol production, as seen over Au/HZSM-5 with carbon additives.²⁰

In this study, we have developed Pd based catalysts for the MtM reaction in a liquid-phase environment, particularly in the presence of H₂O₂ and H₂O. These catalysts are synthesized using a straightforward mechanochemical method,^{21–23} enhancing the formation of a stable and active interfacial carbon (iC) layer. This iC layer creates a distinctive Pd-iC-CeO₂ interface, a pivotal element in preventing the over-activation of hydrogen peroxide and modulating the overall oxidative potential of the catalyst to promote liquid oxygenate products, chiefly methanol. Our research employs in situ attenuated total reflectance infrared spectroscopy (ATR-IR), X-ray photoelectron spectroscopy (XPS), near-edge X-ray absorption fine structure spectroscopy (NEXAFS), and X-ray absorption spectroscopy (XAFS). Additionally, we integrate a comprehensive understanding of the reaction profile through density functional theory (DFT) calculations. The primary focus of our study centers on exploring the impact of the metal–carbon-oxide interface in mechanochemically prepared Pd acetate-CeO₂ catalysts, denoted as Pd-iC-CeO₂.

RESULTS AND DISCUSSION

Catalytic Performance of Pd-iC-CeO₂: Balancing Methane Oxidation and H₂O₂ Decomposition. Pd-iC-CeO₂ shows a 100% selectivity toward methanol at 75 °C (Figure 1A), with no detectable formation of additional oxygenate species. Upon heating to higher temperatures, the reaction favors the production of formic acid, HCOOH, and carbon dioxide, CO₂, without the observation of complex oxygenates such as CH₃OOH and dimethyl ether for the milled catalyst (Table S1). The general trend in reactivity as a function of temperature shows that, as the temperature increases, there is a sequential increase in higher order oxygenates following the trend of CH₄ > CH₃OH > HCOOH > CO₂ under the given reaction conditions with a corresponding increase in the overall rate of methane reaction, indicated by the cumulative increase in total products. The

novelty inherent in the Pd-iC-CeO₂ catalyst lies in the formation of a unique Pd-iC-Ce interface, which plays a crucial role in dampening the hydrogen peroxide decomposition rates and subsequent formation of higher-order oxygenates. In the absence of the iC layer, Pd-CeO₂ shows no selectivity toward methanol at 75 °C and minimal liquid oxygenates at 110 °C (Figure 1B).

Notably, the Pd-iC-CeO₂ catalyst exhibits a hydrogen peroxide decomposition rate that is a factor of 1.5 lower than that of the conventional Pd-CeO₂ catalyst (Figure 2),

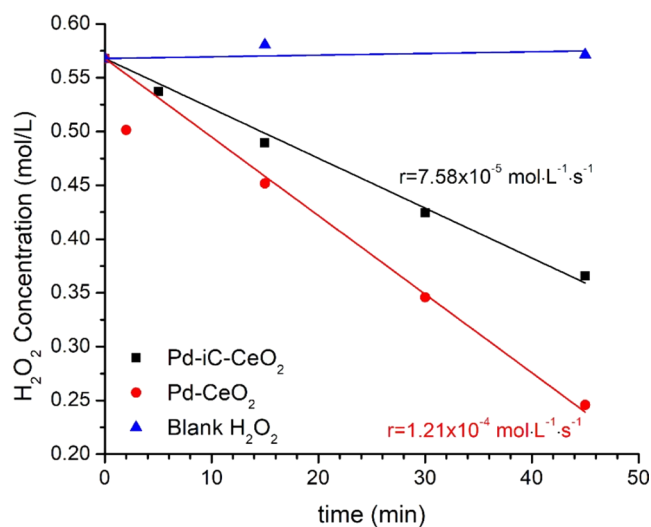


Figure 2. Experimental H₂O₂ decomposition rates evaluated at ambient pressure and temperature over Pd-iC-CeO₂, Pd-CeO₂, and blank H₂O₂ (absence of catalysts) in air. H₂O₂ concentrations are determined via acidified cerium(IV) sulfate titration.

with the rate of peroxide decomposition of 7.58×10^{-5} vs $1.21 \times 10^{-4} \text{ mol/L/s}$ on Pd-iC-CeO₂ and Pd-CeO₂, respectively. The carbon present in the Pd-iC-CeO₂ interface blocks sites involved in the decomposition of H₂O₂, consistent with the theoretical results that will be presented later, which revealed not only a factor of 2.5 stronger H₂O₂ binding on Pd-CeO₂ compared to Pd-iC-CeO₂ (−1.27 vs −0.50 eV for Pd-CeO₂ and Pd-iC-CeO₂, respectively) but also a factor of 1.14 times

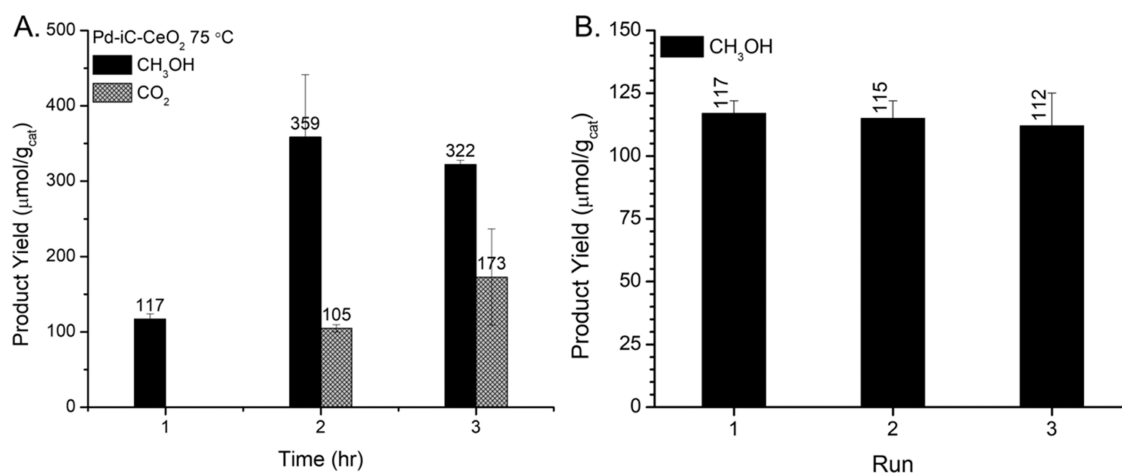


Figure 3. Direct methane to methanol stability testing over Pd-iC-CeO₂ (A) time dependent product yield at 75 °C for Pd-iC-CeO₂ from 1–3 h, (B) recyclability tests at 75 °C for Pd-iC-CeO₂. Reaction conditions: 25 mg of catalyst, 15 mL of 0.5 M H₂O₂ (aq), 20 bar initial pressure of 20% CH₄ in Ar balance, 800 rpm mixing.

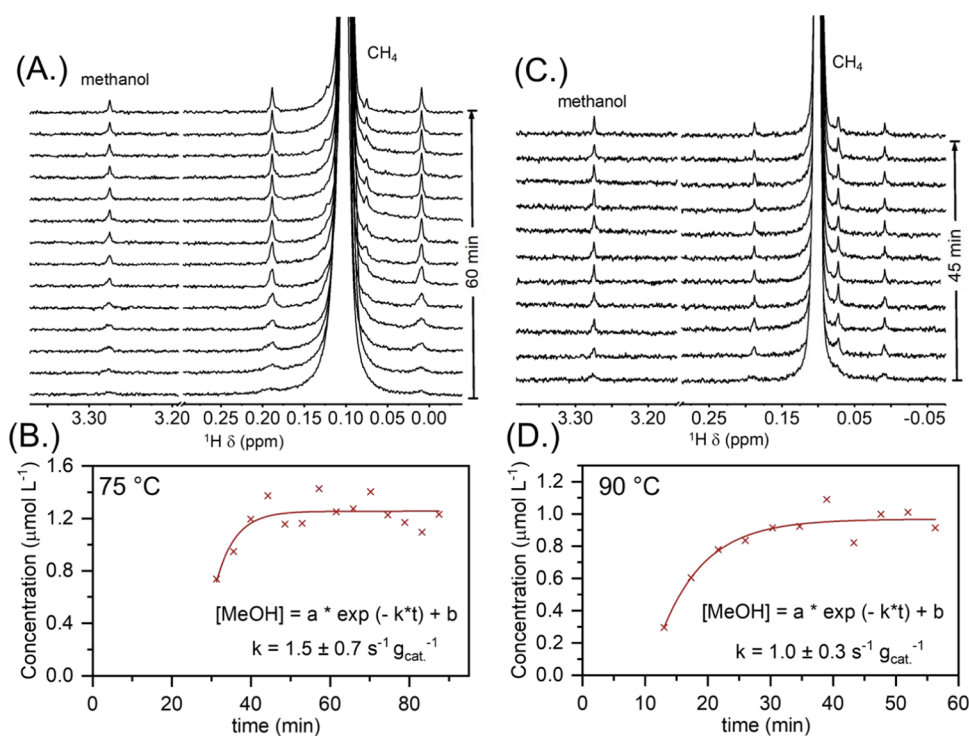


Figure 4. In situ solution NMR studies of direct methane to methanol reaction over Pd-iC-CeO₂. Arrays of the ¹H NMR spectra (4 min 13 s per spectrum) at (A) 75 and (C) 90 °C. Kinetic analysis of time-resolved NMR spectra at (B) 75 and (D) 90 °C. The first-order rate law was assumed to curvefit the time-resolved concentration profile to obtain the rate constant. Reaction conditions: Pd-iC-CeO₂ catalyst (2.3 mg), 0.5 M H₂O₂ in H₂O/D₂O solution (3% H₂O; 97% D₂O; 400 μL), 5 bar methane, 75 or 90 °C.

stronger exothermicity in the H₂O₂ to 2OH reaction. Consequently, this leads to a reduced availability of oxidant for the decomposition of methanol. The ability to independently tune the H₂O₂ decomposition rate and the CH₄ activation cycle is critical to achieve ideal selectivity. Through comparative analysis at 75 °C with reference catalysts (Figure S1) the need for the precise moiety of Pd-iC-CeO₂ was expanded by deconvoluting the contributions from each individual component and combination thereof. In this comparison Pd(OAc)₂ highlights the possibility of a palladium acetate species driving the chemistry, which yielded only methoxyperoxyl. Pd-iC-SiO₂, obtained via the mechanochemical

synthesis of Pd-iC with SiO₂ as the support instead of CeO₂, where SiO₂ is taken to be an inert support, was used to investigate the Pd-iC interface activity without CeO₂, which ultimately favored overoxidation into CO₂. Finally, Pd-CeO₂ assessed the performance of the pure Pd-CeO₂ interface in the absence of the iC interlayer, which led to the lowest selectivity toward oxygenates and purely CO₂. This underscores the necessity of Pd, carbon, and CeO₂ synergy at the Pd-iC-CeO₂ interface for selective methanol formation, where the protection of methanol is often stated as a critical process parameter,²⁴ here we present the possibility of dampening the oxidative potential of the site itself via the incorporation of

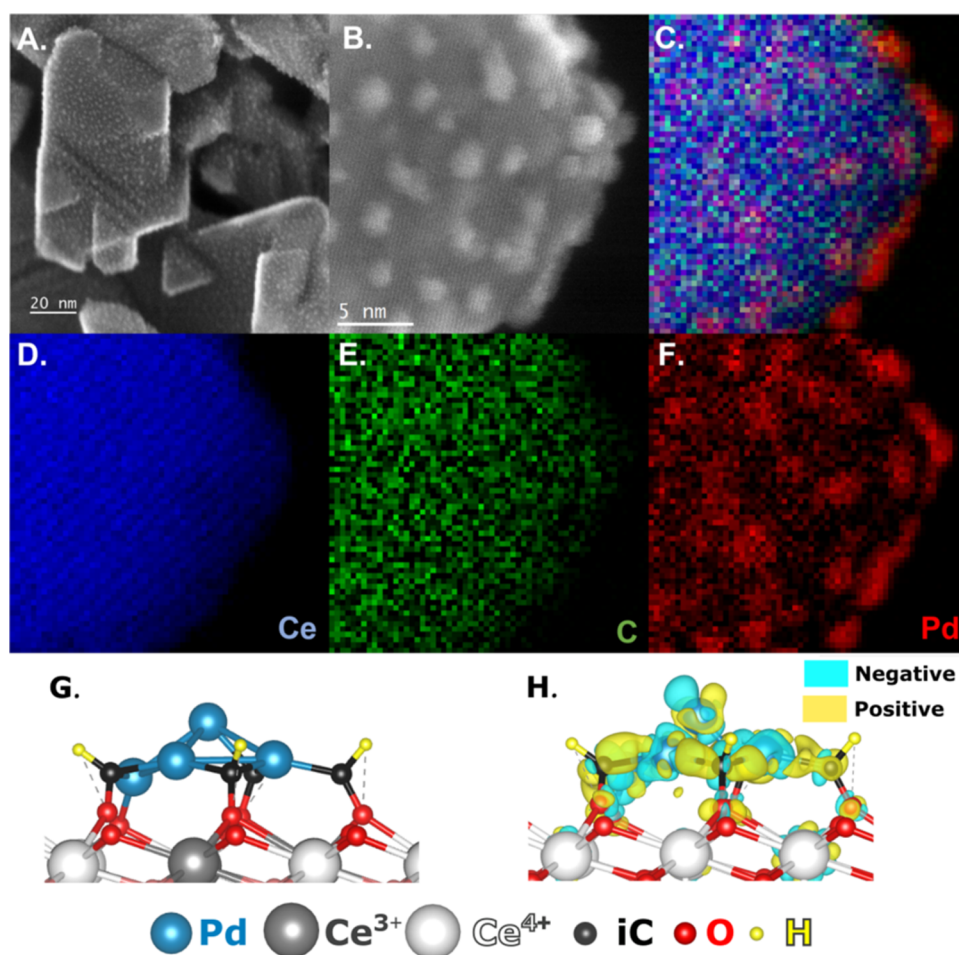


Figure 5. Secondary electron (SE) STEM imaging of Pd-iC-CeO₂ for (A) after 3 consecutive reaction cycles (B) STEM-EELS inset (C) STEM-EELS combined elemental mapping, (D–F) Ce, C, and Pd elemental mapping, respectively. Reaction conditions: 25 mg of catalyst, 75 °C for 1 h, 15 mL of 0.5 M H₂O₂ (aq), 20 bar initial pressure of 20%CH₄ in Ar balance, 800 rpm mixing. Theoretical model of Pd-iC-CeO₂ showing the (G) side view and (H) charge density difference plot, positive/negative differences are visually represented with yellow/cyan, respectively. Color coding: Pd atoms are light blue, Ce⁴⁺ white, Ce³⁺ gray, O atoms of the first layer red, while those of the second layer are light red, iC atoms black and H atoms yellow.

interfacial carbon (iC) to promote selective conversion toward methanol. This results in a novel catalyst interface that yields competitive rates of reaction with other state-of-the-art methane to methanol catalysts, shown in Table S2.^{3,4,8,14,25}

Moreover, the product distribution as a function of time (Figure 3A) exhibits the expected increase in methanol yield. However, with prolonged reaction time, selectivity diminishes, attributed to the formation of CO₂, which is likely due to either exposure of distinct active sites or sequential overoxidation. The plateaued methanol production rate was corroborated via in situ ¹H NMR which monitored the methanol production rate in a methane pressurized sealed NMR vessel, modeling the batch reactor configuration at 75 and 90 °C (Figure 4A,C), which showed that after 1 h under reaction conditions at 75 °C the methanol reaches a maximum (Figure 4A). The first-order fitted rate constant for methanol production via in situ NMR was found to be 1.5 ± 0.7 and 1.0 ± 0.3 s⁻¹ g_{cat}⁻¹ for 75 and 90 °C, respectively (Figure 4B,D), where the induction period before data collection represents the system coming up to temperature. The decrease in the methanol rate constant is consistent with the kinetics which show that the rate of methanol production decreases at 90 °C, in favor of CO₂ production, where the rate constants are derived from in situ

NMR are based on methanol production rate, not total CH₄ rate of reaction. This highlights that the methanol does not appreciably decrease as a function of time, indicating it is not oxidized into higher order oxygenates and/or combustion products sequentially but rather combustion occurs rapidly over distinct active sites that differ from the sites required for methanol formation. This further highlights the importance of not just protecting the methanol intermediates²⁴ but the active site itself to preserve the favorable surface motifs. Notably, the beneficial properties of the mechanochemically prepared Pd-iC-CeO₂ catalyst persist through multiple catalytic cycles (Figure 3B), where the activity remains within error of 117 ± 10 μmol/g_{cat}. The catalyst consistently maintains 100% methanol selectivity even after three consecutive reaction cycles, highlighting the absence of significant Pd leaching. This absence is crucial, as Pd leaching could otherwise lead to a substantial loss in reactivity. Furthermore, the catalyst's dispersion remains largely unchanged, starting at 22% and decreasing to 17% after 3 h reaction time, suggesting that the change in reactivity results from changes in the nature of the active site, rather than merely the number of sites.

Direct Influence of iC Layer on Pd-iC-CeO₂ for Methane to Methanol Reactivity. The distinctive Pd-iC-

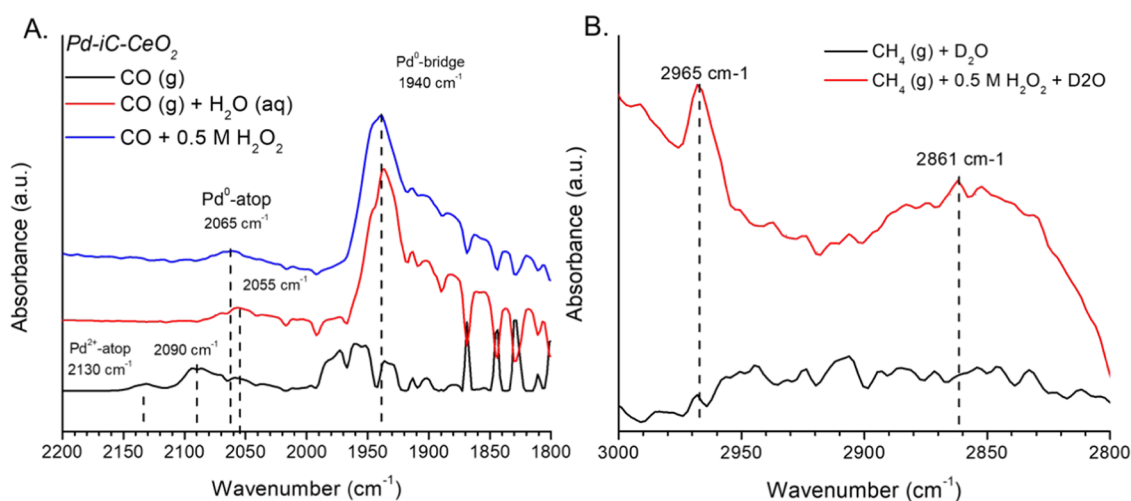


Figure 6. Influence of chemical environment on the surface structure of Pd-iC-CeO₂. (A) CO-ATR of Pd-iC-CeO₂ under pristine, aqueous, and 0.5 M H₂O₂ solutions (B) ATR deconvolution of individual MtM surface states at temperature after simulated reaction conditions in either pure D₂O or 0.5 M H₂O₂/D₂O conditions. Conditions: 10%CO/He or pure CH₄ using 2 mL of D₂O or 0.5 M H₂O₂ in a trough configuration measured in a static gas atmosphere simulating batch condition, conditions for reaction 10 mg catalyst suspended in either D₂O, 0.5 M H₂O₂, or mixtures of D₂O/H₂O₂, as indicated, and reacted in sealed ATR cell under 20 psig gas pressure for 1 h.

CeO₂ interface (Figure 5A–F) is highly stable, shown by the intimate contact between the Pd, Ce, and iC species being preserved after three consecutive reaction cycles. The migration of the iC layers toward the Pd is dependent on the reaction time, where after the optimized 1 h reaction time the catalyst structure is largely preserved (Figure S2), but after a 3 h reaction time the carbon is notably seen to migrate specifically toward the Pd, encompassing the metal and segregating from the CeO₂ (Figure S3). This segregation of the iC layer toward Pd, resulting in the absence of Pd-iC-CeO₂ interface is consistent with the observed CO₂ formation in control experiments where the Pd-iC layer and Pd-CeO₂ were probed in isolation (see Figure S2), promoting increased CO₂ formation. This reflects the loss of the Pd-iC-CeO₂ moiety, favoring the formation of surface Pd-iC, where the Pd-CeO₂ interface is diminished due to carbon migration onto the Pd. Additionally, the exfoliation of the Pd particles is observed over time, with a decrease in wetting of Pd onto the CeO₂ support, accompanied by a 30% increase in particle size from 1.8 to 2.4 nm (Figure S4). The palladium particles remain in an amorphous state, confirmed by powder X-ray diffraction (pXRD), which shows no Pd diffraction (Figure S5). Ostwald ripening, evident from the broadened Pd size distribution, is identified as the mechanism for particle growth, possibly resulting in the trapping of Pd adatoms on the CeO₂.²⁶

To discern the influence of the iC layer in Pd-iC-CeO₂, the iC layer was systematically removed via an oxidative pretreatment at 500 °C under air (Figure S6), resulting in a decomposed Pd-CeO₂ interface that is easily destabilized after reaction (Figures S6 and S7). In line with our evidence that the Pd-iC-CeO₂ dampens H₂O₂ decomposition, the removal of the iC layer via oxidative treatment led to the significant evolution of H₂O₂ into O₂ (g), even at room temperature. Consequently, this inhibited methanol formation at 75 °C due to the absence of available reactive oxidants. After this treatment, Pd-iC-CeO₂ displays no activity for methane partial oxidation to either CO₂ or oxygenates, as the C interlayer is stripped, evidenced by thermogravimetric analysis (TGA) analysis (Figure S8). To rule out the possibility of the iC layer independently reacting with H₂O₂ to yield oxygenates,

which have been reported to participate in the MtM reaction to form oxygenates in carbon containing materials,²⁰ the reaction was conducted under identical reaction conditions but pressurized with Argon instead of CH₄, making iC the only potential source of carbon, which resulted in no oxygenate or CO₂ formation. This finding indicates that the interfacial carbon was not being consumed to form product, highlighting the importance of synchronizing both the catalytic pathways of H₂O₂ decomposition and methane activation while tailoring the active site to favor selective methanol production. In an effort to enhance the selective conversion of methane to methanol and synchronize H₂O₂ evolution, secondary metals are often employed alongside Pd, such as AuPd,^{14,27} or MPd (M = Cu, Ni, Mn, Au),²⁸ resulting in increased reactivity toward oxygenates.

Surface Intermediates of Pd-iC-CeO₂ during Realistic Solvated Methane to Methanol. The pertinent surface chemistry of Pd-iC-CeO₂ has been investigated through in situ attenuated total reflection infrared spectroscopy (ATR-IR) to explore reaction intermediates (Figure 6). Room temperature, ambient pressure CO-ATR spectra of Pd-iC-CeO₂ were obtained in different environments: dry CO, a catalyst slurry in deionized water, and a catalyst slurry containing 0.5 M H₂O₂ (aq) in water (Figure 6A). In dry CO, the formation of highly dispersed Pd²⁺ species at 2130 cm⁻¹, along with atop Pd⁰ sites at 2090 cm⁻¹ and bridge sites at 1970 cm⁻¹ is observed.²⁹ However, in the presence of water and hydrogen peroxide, the Pd²⁺ atop sites transitioned to atop Pd⁰ at ~2060 cm⁻¹, and bridge sites shifted to 1940 cm⁻¹. These changes are attributed to the solvent effects of water on the dipole moment of CO, a phenomenon typically observed in CO-ATR in contrast to gas phase diffuse reflectance infrared Fourier transform spectroscopy (DRIFTS) measurements.³⁰ The formation of reduced Pd-CO species is attributed to the surface reduction as a result of exposure to CO, despite no reductive pretreatment before measurement and the catalysts being used as is after drop casting. This is consistent with the formation of bridge and hollow sites on ~1.7 nm particles of Pd, even in the presence of a solvent (J. Cat., 2002, 210, 160–170). To isolate the effects of water and hydrogen peroxide, and remove

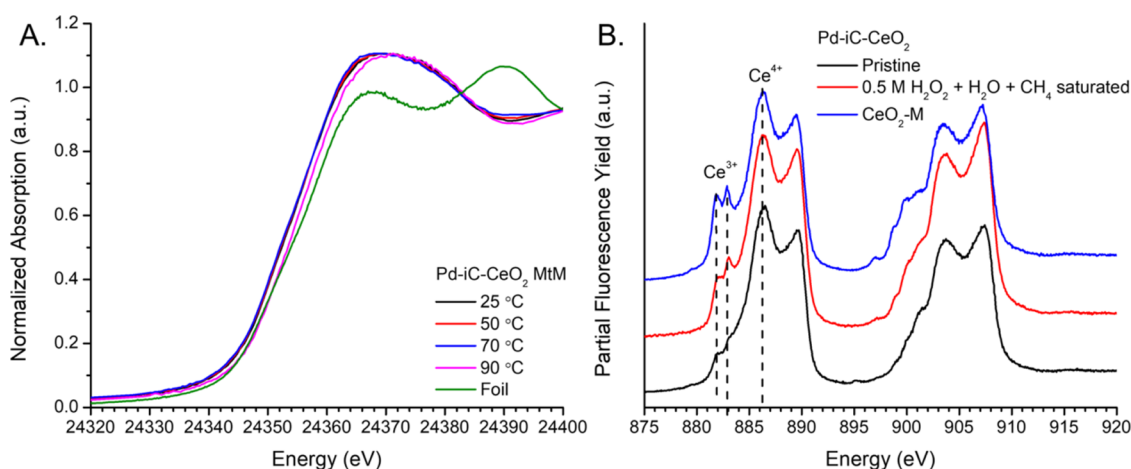


Figure 7. Formal oxidation state of Pd-iC-CeO₂ in H₂O₂(aq) solvated conditions (A) Pd-K edge XAFS under high pressure methane to methanol conditions (34 bar total pressure, 20 bar CH₄ pressure, 0.01 M H₂O₂ with 0.1 mL/min flow). (B) Ce M_{4,5}-edge NEXAFS spectra comparing CeO₂-M sample, pristine Pd-iC-CeO₂, and Pd-iC-CeO₂ in the reaction solution measured using a static NEXAFS liquid cell charged with Pd-iC-CeO₂ in 20 μ L post reaction liquor after 1 h under MtM conditions.

contributions from broad OH bands, mixtures of D₂O and D₂O/H₂O₂ were used to access the MtM C-H reactive intermediates (Figure 6B). In the presence of the oxidant, H₂O₂, characteristic methoxy bands at 2965 and 2860 cm⁻¹ appeared,^{3,8,31} reflecting successful conversion of methane into methanol. Notably, the catalyst shows methoxy formation even at the operating pressure of the ATR, which was approximately 20 psi CH₄ partial pressure, which is in agreement with the findings from the catalytic reactor which operated at \sim 4 bar (56 psi) CH₄ partial pressure. In contrast, these bands did not appear in the case of CH₄ + D₂O alone, demonstrating that water alone is insufficient to activate the reaction due to the catalyst's inability to dissociate D₂O on its own. Furthermore, in the presence of 0.5 M H₂O₂ + D₂O, the scrambling of H-O-H, H-O-D, and D-O-D bands at 1650, 1470, and 1290 cm⁻¹, respectively (Figure S9), suggests that dissociated H₂O₂ rapidly complexes with deuterated water.³² This indicates that while water may not directly contribute to the methanol catalytic cycle, it plays an essential role in replenishing oxygen vacancies, recombining with peroxide, and providing surface OH sites. Hydrogen peroxide and peroxy radicals (OOH) are also observed at 3210 cm⁻¹ and as a shoulder at 1420 cm⁻¹ in the deuterated case, attributed to the unique cyclic recombination of HOOH-HOO species, which readily form complexes.^{32,33} CO-ATR following an in situ MtM reaction treatment at 75 $^{\circ}$ C (Figure S10) showed that both the presence of water and 0.5 M H₂O₂ (aq) did not affect the surface Pd adsorption sites. Atop and bridge Pd⁰ sites at 2051 and 1928 cm⁻¹, respectively, were preserved relative to the room temperature CO-ATR. The shift of atop CO in 0.5 M H₂O₂ from 2060 to 2050 cm⁻¹ is attributed to the decomposition of H₂O₂ after the reaction, where the H₂O₂ is rapidly consumed at 75 $^{\circ}$ C, where the absence dipole-dipole interactions between H₂O₂ derived radicals and CO, causes a shift to lower wavenumber after the H₂O₂ has been consumed,^{30,32} where post reaction acidified ceric sulfate titration has shown that the H₂O₂ is fully consumed upon completion of the reaction at 75 $^{\circ}$ C over Pd-iC-CeO₂, where H₂O₂ decomposes into O₂ and H₂O. The preservation of the CO-Pd sites on the pristine material (Figure 6A) at room temperature versus after in situ reaction, measured at 75 $^{\circ}$ C (Figure S10), shows that the relevant active sites are preserved

after reaction, consistent with the STEM imaging showing the Pd-iC-CeO₂ moiety is preserved.

Structural and Surface Analysis of Pd-iC-CeO₂ via In Situ Methane to Methanol Conditions. In situ solvated X-ray absorption spectroscopy (XAS) and static solvated phase near edge X-ray absorption spectroscopy (NEXAFS) were carried out to determine the state of Pd and Ce, in the true reaction media of 0.5 M H₂O₂ (aq). The Pd K edge of Pd-iC-CeO₂ (Figure 7A), measured in situ at the high-pressure liquid-gas-solid interface at 34 bar using a CH₄ saturated (20 bar CH₄ partial pressure) solution of 0.01 M H₂O₂ (aq), captures the true solvent effects of the aqueous reaction at pressures relevant to the reactor studies. The introduction of the reaction mixture shows that the system is stable up until 70 $^{\circ}$ C, beyond which the catalyst begins to be reduced toward a lower oxidation state, as evidenced by a shift in the white line to a more reduced Pd state relative to the pristine material, while the other temperatures have no discernible difference with the pristine material. Under methane-saturated water in the absence of the oxidant, H₂O₂, Pd-iC-CeO₂ did not experience a notable shifting of the white line as a function of temperature, only minor changes above the edge (Figures 7A and S11). However, upon addition of the oxidant, H₂O₂ (Figure S11A), there is a shift to a more oxidized state of Palladium which is reversed upon reaching 90 $^{\circ}$ C, mirroring the X-ray absorption near edge structure (XANES) of the system without oxidant (Figure S11B), likely due to the rapid decomposition of H₂O₂ that is also coupled to the onset formation of higher order oxygenates, i.e., CO₂. Conversely, Pd-CeO₂ exhibits no redox behavior during methane-to-methanol conversion in the presence of H₂O₂ or under the presence of CH₄-saturated water at any temperature (Figure S12). Based on the findings from the Pd-iC-CeO₂ XANES and the relative rates of peroxide decomposition of both systems this is likely due to the rapid decomposition of H₂O₂ over Pd-CeO₂ which results in both systems appearing identical both with and without oxidant, as a mixture of O₂ and H₂O, the total H₂O₂ decomposition products, create a milder oxidizing environment than partial decomposition of H₂O₂ in the form of OH and OOH. XPS analysis indicates that the

surface is primarily Pd⁴⁺, consistent with PdO₂ species (Figure S13), in agreement with the Pd K edge showing a formal oxidation state >2. The minority species in the XPS, Pd²⁺, is likely an undercoordinated surface facing site that is ultimately reduced during Pd-CO ATR-IR to form an overlayer of $n > 2$ CO-Pd sites. However, XPS was measured under ex situ UHV conditions, while nominal exposures of CO to Pd can result in surface reduction even at low partial pressures of CO (Chem. Phys. Lett. 1990, 5(6), 391–398), where CO-ATR was measured at 827 Torr CO (16 psi total pressure). The Pd 3d to C 1s ratio (Pd/C) of approximately 1:1.5 on the surface (Figure S13) shows that the carbon species retains its acetate-derived C_xO_yH features at 289 eV, enabling unique surface chemistry compared to inert C* species. Moreover, the C 1s spectrum shows that the acetate-derived features remain present even after the reaction (Figure S13). The combination of XAFS, XPS, and CO-ATR illustrate the need for various spectroscopic techniques to probe the multivalent surface/structure, showing the bulk properties, the reactive species which bind to CO and the subtle shift in surface structure under pristine conditions via XPS. The key findings from in situ XANES during MtM is that as the temperature is increased, the peroxide decomposes rapidly, resulting in the reduction of the Pd sites toward metallic Pd⁰ at 90 °C, which is correlated to the onset formation of CO₂ to the presence of metallic Pd⁰ sites.

The influence of Ce was explored via Ce M_{4,5} Edge NEXAFS performed in a solvated static reaction cell to simulate batch reaction conditions (Figure 7B), which was measured at atmospheric pressure using a 20 μL aliquot of post reaction liquor and post reaction Pd-iC-CeO₂ which was carried out in the high-pressure batch reactor under identical conditions as the kinetic measurements. Pure CeO₂-M, milled CeO₂ in the absence of Pd, shows lower-energy Ce³⁺ features at 882.0 and 882.9 eV³⁴ due to the formation of defect sites during mechanochemical synthesis. The incorporation of Pd onto CeO₂-M shows a decrease of the Ce³⁺ peaks, indicating that these defect sites are occupied by the intermediate Pd(OAc)₂ precursor and eventual Pd-iC moiety. During in situ conditions, the Ce³⁺ peaks at ca. 882.0 and 882.9 eV suggest that defect sites, in addition to the Pd-iC-CeO₂ moiety, are involved in the reaction, likely in the form of oxygen vacancies that can be readily saturated by the solvent. The NEXAFS Ce M_{4,5} was corroborated with post reaction XPS showing the Ce 3d spectra with primarily Ce⁴⁺ with a trace amount of Ce³⁺ (Figure S14). The evidence from NEXAFS and XAS supports the hypothesis that Pd-iC-CeO₂ is modified by iC, which modulates the charge of Pd shown via charge distribution plots (Figure 5G,H), and ultimately dampens formation of CO₂ and H₂O₂ decomposition, giving greater insights into the kinetic measurements by linking the increase in deep oxidation products (HCOOH, CO₂) as a function of temperature to a reduction of Pd.

DFT Modeling of Methane Activation and H₂O₂ Activation over Pd-iC-CeO₂. Density functional theory (DFT) was employed to elucidate the nature of the active sites responsible for the exclusive selectivity toward methanol. Two distinct models were created: one involving the adsorption of a rhombohedral Pd₄ cluster adsorbed on plain CeO₂(111), denoted as Pd-CeO₂ (Figure S15), and the other one created by adding four C-H species to Pd-CeO₂ to represent the Pd-iC-CeO₂ interface (Figures 5G and S15). C-H bonds were introduced into the model to stabilize the

carbon species, recognizing that under experimental conditions, carbon is likely to be hydrogenated due to the presence of the solvent. In the Pd-CeO₂ model, the four Pd atoms collectively transfer one e⁻, resulting in the reduction of one Ce⁴⁺ ion to a Ce³⁺ species. However, in the Pd-iC-CeO₂ model, each of the four C atoms transfers one e⁻, leading to the formation of four Ce³⁺ species, while the Pd₄ nanostructure, similar to the Pd-CeO₂ case, donates another e⁻, forming a fifth Ce³⁺ species. The Bader charge analysis indicates that the Pd atoms are partially oxidized, as shown in Figure S15. The Pd/C:1 ratio used in the Pd-iC-CeO₂ model catalyst in the DFT calculations closely matches the experimentally determined surface composition obtained via XPS. Test models with Pd nanoparticles approximately 1 nm in size have been calculated, and the activation of CH₄ and H₂O₂ has been studied, yielding results similar to those obtained with the four-Pd models. This indicates that these models capture the essential physicochemical properties of the metal-(iC-) oxide interfaces.

The independent activation of H₂O₂ and CH₄ was explored for both models (Figures S16–S17, respectively). These investigations revealed that, on Pd-iC-CeO₂, the adsorption of H₂O₂ is approximately 0.8 eV weaker compared to Pd-CeO₂, and the H₂O₂* → 2OH* decomposition reaction is 0.4 eV less exothermic (Figure S16), consistent with experimental work showing Pd-CeO₂ has a 22% higher rate of decomposition than Pd-iC-CeO₂. Furthermore, on Pd-iC-CeO₂, the adsorption of CH₄ is approximately 0.6 eV weaker compared to Pd-CeO₂. Pd-CeO₂ exhibits higher activity in cleaving of the first C-H bond in CH₄*, with a 0.7 eV lower activation energy barrier compared to Pd-iC-CeO₂ (Figure S17). Examining the geometry of the molecular states of H₂O₂* and CH₄* on Pd-CeO₂ and Pd-iC-CeO₂, it is observed that the H-Pd and C-Pd distances in both molecular states are shorter in Pd-CeO₂ compared to Pd-iC-CeO₂ (Figures S16 and S17).

Influence of the Carbon Interface on Ligand Effect and Strong Metal-Support Interaction (SMSI) in Pd-Based Catalysts. Our study demonstrates the significant influence of the carbon interface on the adsorption and activation processes of H₂O₂ and CH₄ species on Pd-based catalysts, highlighting the roles of ligand effect and strong metal-support interaction (SMSI). Charge difference plots (Figures 5H and S18) further illustrate distinctions between the Pd-CeO₂ and Pd-iC-CeO₂ models. Analysis of the molecular states of H₂O₂* and CH₄* on Pd-CeO₂ and Pd-iC-CeO₂ (see Figure S19), reveals notable differences in the H-Pd and C-Pd distances. In Pd-CeO₂, these distances are shorter, facilitating easier molecule activation. This phenomenon is attributed to the ligand effect, where the CeO₂ support withdraws electron density from Pd atoms, promoting an attractive molecule-surface interaction and facilitating bond cleavage, as previously reported.³³ In the case of H₂O₂ adsorption, the O-Pd bond length is 202 pm for Pd-CeO₂ and 219 pm for Pd-iC-CeO₂ (Figure S19). This 17 pm bond length difference results in distinct charge transfer dynamics. In Pd-CeO₂, charge predominantly transfers to an oxygen atom in the CeO₂ support, with only 10% transferred to the H₂O₂ molecule, while the remainder goes to the oxide. In contrast, in the Pd-iC-CeO₂ system, the entire charge transfers to the H₂O₂ molecule, highlighting the role of the carbon interface in facilitating complete charge transfer to the adsorbed molecule.

Similar geometrical trends are observed in the adsorbed state of CH₄ (Figure S19g–j). In Pd-CeO₂, there is a noticeable 6

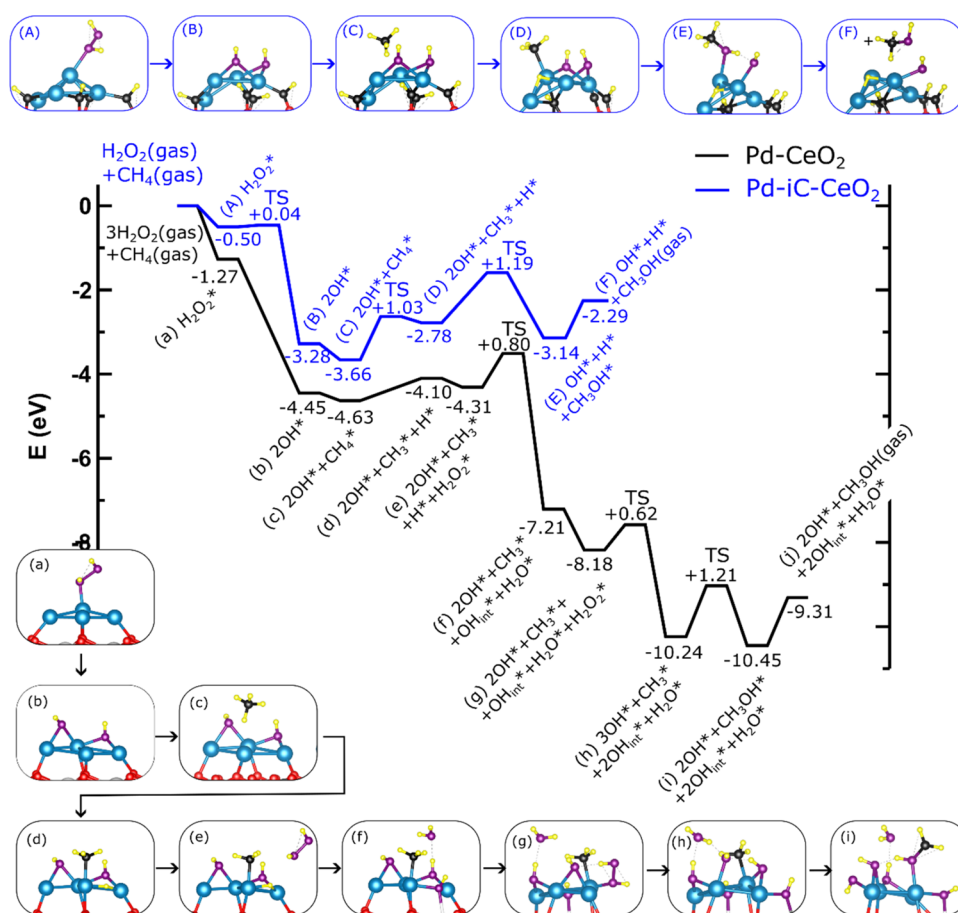


Figure 8. Mechanisms for methanol formation on Pd-iC-CeO₂ (A–F, blue path) and Pd-CeO₂ (a–i, black path) catalysts. The same color coding is used as in Figure 5, additionally the O atoms from the H₂O₂ species are denoted in violet.

pm elongation in the C–H bond, whereas in Pd-iC-CeO₂, this elongation is only 1 pm. Charge analysis reveals that CH₄* donates approximately 0.1e⁻ to Pd-CeO₂, which is accepted by the oxide support. In contrast, on Pd-iC-CeO₂, only 0.03 are donated, with the charge is entirely transferring to the Pd nanoparticle, indicating that the carbon interface acts as a barrier for charge transfer to the oxide. Moreover, the d_{z²}-projected density of states on the Pd atom, where CH₄ adsorbs, reveals an occupancy of 71.5% in Pd-CeO₂ and 98.2% in Pd-iC-CeO₂ (Figure S20). The lower d_{z²} occupation in the Pd-CeO₂ is attributed to ligand effects, highlighting that the CeO₂ support withdraws electron density from the Pd atoms.

Finally, in the case of 2OH groups adsorbed on the Pd nanoparticles, charge analysis indicates that the Pd nanoparticle in Pd-CeO₂ donates 0.87e⁻, whereas in Pd-iC-CeO₂, it donates 0.97e⁻. Nearly the entire charge is transferred to the 2OH groups, resulting in excess charges of 0.85 and 0.94e⁻, respectively. This behavior is primarily due to the OH⁻ groups' tendency to capturing charge.

The carbon interface in Pd-iC-CeO₂ restricts charge transfer to the CeO₂, thereby modulating the SMSI. This modulation reduces the interaction between Pd and CeO₂, allowing the Pd nanoparticles to retain more charge and enhancing the overall catalytic performance. Overall, these findings underscore the crucial role of the carbon interface in influencing adsorption geometries, activation energies of reactive species, and charge transfer processes on Pd-based catalysts

Langmuir–Hinshelwood Approximation for Methane to Methanol.

The comprehensive MtM reaction mechanism is compared for both models in Figure 8, following a traditional gas-phase Langmuir–Hinshelwood (LH) mechanism for both Pd-CeO₂ and Pd-iC-CeO₂. The analysis reveals that surface OH* species mainly affect the stabilization of CH₄* species. On Pd-iC-CeO₂, the binding of CH₄* species is 0.2 eV stronger than on Pd-CeO₂ (Figure 8). When OH groups are coadsorbed on Pd-iC-CeO₂, the CH₄ loses 0.01e⁻ of charge compared to the case of CH₄/Pd-iC-CeO₂ without OH groups. This charge is transferred to the OH groups, leading to increased adsorption energy for CH₄ species when coadsorbed with OH species. Conversely, in the (CH₄ + 2OH)/Pd-CeO₂ system, CH₄ gains 0.07e⁻ compared to the CH₄/Pd-CeO₂ case without OH groups. The charge on the OH groups and the Pd nanoparticle remains unchanged. This indicates that the charge gained by CH₄ is transferred by the CeO₂ support. Therefore, as CH₄* becomes more charged, the adsorption energy decreases. Additional analysis further confirms that on both Pd-CeO₂ and Pd-iC-CeO₂ surfaces, the rate-limiting step is the formation of CH₃OH* (*E*_{act} = 1.21 and 1.19 eV, respectively). The presence of carbon may act as passivating agent for Pd, resulting in reduced overoxidation, similar to the effect observed for Cu–Ag interfaces, where the presence of a unique bimetallic site was necessary to favor liquid oxygenate yield.¹⁸ Notably, in the case of Pd-iC-CeO₂, CH₃OH* is formed from CH₃* and OH* species immediately following the dissociation of CH₄* (Figure 8). In contrast, the same step

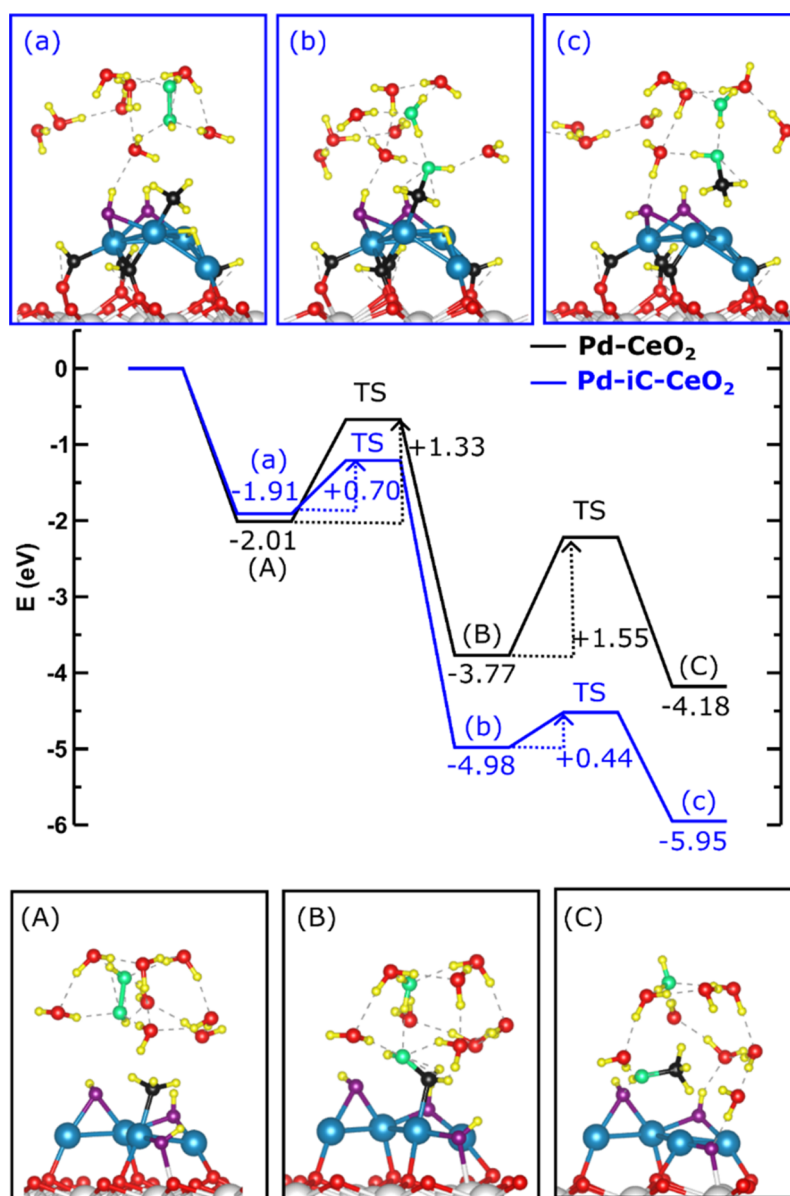


Figure 9. Eley–Rideal type mechanism for the formation of CH_3OH on Pd-CeO_2 (A–C, black path) and Pd-iC-CeO_2 (a–c, blue path). The first step of the mechanism involves the formation of CH_2OH and then the formation of CH_3OH . The adsorption energy of each stable state and the activation energy associated with the transition states relative to their precursor states are included.

on Pd-CeO_2 would have a higher activation barrier of 1.53 eV (Figure S21). However, this barrier can be reduced by adding H_2O_2 molecules, where Pd-CeO_2 consumes three H_2O_2 molecules (Figures 8 and S21–S22) while Pd-iC-CeO_2 only requires one H_2O_2 molecule to drive the reaction forward (Figures S23–S24). This comparison reveals that the presence of carbon at the interface of the hydroxylated surface has a dual effect: it favors the stabilization of the methane but also blocks sites where highly oxidizing OH_{int} species form. This is notably in agreement with the experimental reduced rate of H_2O_2 decomposition.

Modeling Solvent Effects via Eley–Rideal-like Mechanism on Pd-Based Catalysts. The effect of hydrogen peroxide in an aqueous medium was also considered to analyze an Eley–Rideal-type mechanism, in which CH_3OH is formed through the interaction of CH_3^* with OH from the aqueous phase. The initial-state structures chosen for this study are shown in Figure S25. For Pd-iC-CeO_2 , the starting point is

adsorbed $\text{CH}_3^* + \text{H}^* + 2\text{OH}^*$ (states shown in Figures 8D and S25), whereas for Pd-CeO_2 , we begin with $\text{CH}_3^* + 2\text{OH}^* + \text{OH}_{\text{int}}^*$ (state in Figure 8f without the H_2O^* molecule). The selection of different degrees of hydroxylation was based on the fact that Pd-CeO_2 was more prone to hydroxylation.

Hydrogen peroxide in an aqueous medium was modeled by including the $8\text{H}_2\text{O} \cdot 2\text{OH}(\text{aq})$ complex, as shown in Figure S25. In the case of Pd-iC-CeO_2 , this aqueous complex was adsorbed onto the previous model ($\text{CH}_3^* + 2\text{OH}^* + \text{H}^*$)/ Pd-iC state (resulting in new states, as shown in Figures 9a and S26). As can be seen, 2OH eventually formed H_2O_2 . Then, $\text{H}_2\text{O}_2(\text{aq})$ is activated to $2\text{OH}(\text{aq})$, where one $\text{OH}(\text{aq})$ breaks the C–Pd bond, forming an unstable CH_3OH . The C–H and O–H bonds are then broken, where one H binds to the Pd nanoparticle and the other H forms an H_2O molecule with the remaining $\text{OH}(\text{aq})$, leaving an unstable CH_2O^* species. Finally, the H atom initially bound to the Pd nanoparticle binds to the O atom of CH_2O , forming CH_2OH^* , with an

overall barrier of 0.70 eV (see Figure S26 top panel). In contrast, the formation of CH_2OH^* on Pd-CeO₂ with the 8H₂O·2OH(aq) moiety results in a barrier of 1.33 eV (Figure 9), which includes the formation of 2OH species from H₂O₂, formation of CH₃ and the corresponding H* abstraction, and the final CH₂OH formation. This significant difference is due to the different pathways, as explained, where the carbon atom in $\text{CH}_3^* + 2\text{OH}^* + \text{H}^*$ on Pd-iC-CeO₂ (see Figure 9a) is 0.09e more charged than that in $\text{CH}_3^* + 2\text{OH}^* + \text{OH}_{\text{int}}^*$ on Pd-CeO₂ (see Figure 9A). This results in a C–Pd bond length of 211 pm in Pd-iC-CeO₂ compared to 202 pm in Pd-CeO₂. This difference makes CH₃* on Pd-iC-CeO₂ more labile to C–Pd bond breaking, leading to distinct pathways for CH₂OH formation on each catalyst. Consequently, on Pd-iC-CeO₂, OH(aq) breaks the C–Pd bond, forming unstable CH₃OH species, whereas on Pd-CeO₂, the C–H bond breaks, forming a CH₂ species that is labile to CH₂OH formation. Notably, the CH₂OH species is by 1.21 eV more stable on the Pd-iC-CeO₂ catalyst than on Pd-CeO₂. Furthermore, the formation of CH₂OH on Pd-iC-CeO₂ yields an energy gain of 3.07 eV, whereas on the energy gain Pd-CeO₂ is only 1.76 eV, which is 1.31 eV less.

The last step of the mechanism involves the formation of CH₃OH from CH₂OH, with differences between the two models. In Pd-CeO₂, the hydrogen atom comes from OH_{int}*, whereas in Pd-iC-CeO₂, it comes from the adsorbed H* (see Figures 9 and S27). This difference is due to the Pd-CeO₂ model catalyst being more hydroxylated than Pd-iC-CeO₂, increasing the probability of H* interacting with OH species to form H₂O* and thus decreasing the H* concentration. Breaking the O–H bond is more difficult and leads to a high activation barrier for CH₃OH* formation, $E_{\text{act}} = 1.55$ eV, which is much higher than that of Pd-iC-CeO₂, $E_{\text{act}} = 0.44$ eV.

From these results, it can be concluded that in the case of Pd-iC-CeO₂, the activation barriers are low, and the limiting step is the initial CH₄ activation, requiring 1.03 eV (Figure 9). In the case of Pd-CeO₂, CH₄ activation is facile (0.33 eV), and the highest barriers are found for the formation of CH₂OH and CH₃OH (1.33 and 1.55 eV). This suggests that the limiting step for Pd-CeO₂ is the formation of CH₃OH.

Balancing LH and ER Mechanisms for Direct Methane to Methanol Conversion. In the final step of the MtM reaction, the desorption of CH₃OH plays a critical role. In the LH mechanism (Figure 8), CH₃OH* desorbs with energies of 1.14 and 0.85 eV from the Pd-CeO₂ and Pd-iC-CeO₂ surfaces, respectively, which is associated with the cleavage of a Pd–O bond of 2.08 and 2.19 Å, respectively. However, in the ER mechanism (Figures 9 and S25), the formed CH₃OH(aq) species are already detached from the surfaces, with Pd–O distances of 2.57 and 2.72 Å for the Pd-CeO₂ and Pd-iC-CeO₂ surfaces, respectively. This is a result of the occupancy of the filled states on the Pd site of Pd-iC-CeO₂ as discussed above. Consequently, the presence of the Pd-iC-CeO₂ interface significantly facilitates methanol desorption, and the role of solvation effects is crucial for its effortless removal. This underscores that while water may not be a main reactive species by itself, its function as a carrier for the catalytically relevant OH species is paramount in driving the selective conversion of methane to methanol. These findings align with the existing literature on gas-phase methane to methanol conversion, which highlights the need for water vapor flow to desorb the methanol species. The synergistic effect arising from the presence of carbon at the Pd-iC-CeO₂ interface, and

the influence of solvation effects are the key factors that render the Pd-iC-CeO₂ catalysts highly active and selective for the MtM reaction.

CONCLUSIONS

In summary, this study underscores the pivotal role of modulating the activity of highly active metal-oxide interfaces by the incorporation of carbon interlayers. Particularly in partial oxidation reactions, where the formation of undesirable total oxidation products is a challenge, precise control over the activation of the oxidant and the reactant emerges as a critical factor for achieving highly selective partial oxidation outcomes. Interfacial carbon proves essential for balancing the activation of the oxidant in tandem with the CH₄ to achieve ideal product selectivity. These findings hold the promise of paving the way for cost-effective metal–carbon-oxide catalysts that harness the synergistic properties of reducible oxide supports and highly active metal centers while leveraging unique solvent effects to enhance the production of desired target products. This breakthrough opens new avenues for advancing catalytic process, contributing to sustainable and efficient chemical transformations, and ultimately fostering cleaner and more environmentally friendly chemical industries in the future.

EXPERIMENTAL METHODS

Catalyst Synthesis. The catalysts were synthesized following dry mechanochemical synthesis, outlined in detail elsewhere.²² Briefly, Palladium(II) acetate (Sigma-Aldrich, 99.99%) was mixed with a corresponding amount of a commercial ceria support (Rhodia), previously calcined at 900 °C for 3 h (Brunauer–Emmett–Teller (BET) surface area ≈25 m²/g). The resulting catalyst obtained after the mechanochemical synthesis, referred to as Pd-iC-CeO₂, was used as is, unless otherwise specified. Comparative catalysts were prepared by conventional incipient wetness impregnation,²¹ Pd-CeO₂, and by milling Pd acetate over SiO₂ previously calcined at 800 °C for 3 h (BET surface area 5 m²/g), following the same milling procedure,²¹ and denoted as Pd-SiO₂. All samples have a final nominal Palladium loading of 4 wt %.

Catalytic Performance Evaluation. The methane to methanol experiments were carried out using a commercial Parr autoclave reactor (Parr 5500 Reactor). Typically, 25 mg of catalyst was added to 15 mL of 0.5 M H₂O₂ aqueous solution and stirred at 800 rpm. The sealed solution was flushed with 20% CH₄ balanced in Ar gas mixture 5 times to remove residual air contaminants and then pressurized to 20 bar under the same 20% CH₄ mixture gas (4 bar CH₄, 16 bar Ar). The head gas was continuously analyzed using an online gas chromatography (GC) equipped with TCD/FID (Agilent 7890B) detectors connected directly to the Parr reactor for the analysis of methane and CO₂ before and after the reaction. The reaction solution was rapidly heated to the desired temperature and held for the specified time. Subsequently, the entire Parr reactor was quenched in an ice bath (<10 °C) to prevent further reaction and the volatilization of oxygenate products via flashing. Liquid products were analyzed via ¹H NMR (Bruker AVANCE 400 MHz) using 0.1 mL of 0.1 wt % 3-(trimethylsilyl)-1-propanesulfonic acid-*d*₆ sodium salt (DSS) prepared in D₂O as the locking agent (DSS/D₂O) as an internal standard, along with 0.7 mL of the filtered reactor solution. The ¹H NMR was quantified by calibrating against known standards of the oxygenates relative to the DSS peak. Samples with pretreatment were prepared *ex situ* in a tubular furnace using polished quartz crucibles before charging into the batch reactor. All measurements were performed in triplicate, as batch reactor systems can introduce higher error than traditional gas-phase reactors due to additional preparation steps. Recycle runs from methane to methanol were performed sequentially, with the reactor solution being evaluated after each run. Finally, the catalysts were washed, recovered, and dried in air, where the subsequent cycles were carried out following the same procedure

listed above for a typical reaction. Hydrogen peroxide concentrations were determined via acidified ceric sulfate titration, where the relative rates of peroxide decomposition were carried out at 25 °C and 1 atm pressure under ambient air using 15 mL of ~0.5 M H₂O₂ and 25 mg of catalyst under mixing. Blank H₂O₂ was the relative rate of decomposition of the pure aqueous peroxide mixture in the absence of a catalyst at standard temperature and pressure.

Powder X-ray Diffraction (pXRD). Powder XRD patterns were collected using a Philips X'Pert Diffractometer equipped with an X'Celerator detector, using Ni-filtered Cu K α radiation ($\lambda = 1.542 \text{ \AA}$) operating at 40 kV and 40 mA. Diffractograms were collected in the 20–80° 2 θ range, with 0.02° step size and 40 s counting time per step.

Thermogravimetric Analysis (TGA). TGA experiments were carried out in a Q500 thermogravimetric apparatus (TA Instruments), loading ca. 15 mg of sample in a platinum pan and increasing the temperature at 10 °C/min up to 600 °C under 60 mL/min of air.

Attenuated Total Reflectance Infrared Spectroscopy (ATR-IR). The ATR-IR measurements were conducted on a Bruker Vertex 70 Infrared Bench using a commercial Harrick Horizon Multiple Reflectance ATR cell equipped with a special high pressure and temperature liquid cell, which was constructed from Hastelloy (generic name, Alloy C-276) in all wetted parts to prevent cell degradation under peroxide conditions and adapted for high temperature and pressure, shown in detail in Figure S28. The cell was connected to an MCT detector with a resolution of 4 cm⁻¹. A Si ATR 45° prism was used due to its chemical inertness, as ZnSe decomposes under solvated peroxide conditions. For dry measurements, the catalyst was dropcast directly onto the Si ATR prism using a slurry of catalyst and deionized (DI) water. Gas (He, CO, or CH₄, all UHP) was flowed over the catalyst at the specified temperature at a total flow rate of 20 mL/min. Solvated liquid phase ATR measurements were performed by preparing a slurry of the catalyst in the specified solvent (H₂O, D₂O, 0.5 M H₂O₂ (aq), 0.5 M H₂O₂ in D₂O). This was achieved by dispersing the finely ground catalyst and sonicating the solution for approximately 10 min. The resulting slurry was loaded into the Horizon Cell trough (approximately 1 mL of slurry) and purged with He to remove residual air contaminants. The background of all measurements was taken after He flushing at the specified temperature. For CO-ATR 10%CO/He was used for all CO-ATR measurements in either DI H₂O, 0.5 M H₂O₂ (aq), while UHP CH₄ was used for the simulated methane to methanol conditions using either a mixture of 0.5 M H₂O₂ prepared in H₂O or D₂O, as listed, or purely CH₄ in either H₂O or D₂O. In the case of methane to methanol ATR measurements, the cell was first purged with CH₄ to remove residual inert gas and saturate the slurry. Subsequently, it was sealed and pressurized to approximately ~20 psi of CH₄, and measurements were taken as a function of time. The process was completed with a desorption step in He. The catalyst bed remained wetted throughout the entirety of the experiments, evidenced by remaining liquid upon removing the crystal and sample.

Scanning Transmission Electron Microscopy (STEM). STEM imaging and STEM-EELS were performed using Hitachi HD2700C dedicated STEM with the probe Cs corrector and Gatan Enfium EELS at an accelerating voltage of 200 kV in the Center for Functional Nanomaterials at Brookhaven National Laboratory. All STEM images were acquired with the secondary electron (SE) detector to clearly image Pd nanoparticles on ceria support.

Near Edge X-ray Absorption Spectroscopy (NEXAFS). NEXAFS measurements were carried out at the National Synchrotron Light Source II (NSLS-II) at Brookhaven National Laboratory at the In situ and Operando soft X-ray spectroscopy (IOS) beamline, 23-ID-2. Ex situ measurements were done by dropcasting the powders onto Indium Foil strips prior to loading into the UHV endstation, where the C and O K-edges were measured in addition to the Ce M_{5/4}-edge. In situ measurements were carried out using a custom-built static liquid cell sealed with a 100 nm-thick X-ray transparent Si₃N₄ window. The cell was charged with the catalyst extracted from the Parr reactor at the following operating conditions: 20 bar pressure (20% CH₄), 75 °C, 800 rpm, 15 mL of 0.5 M H₂O₂ (aq), and 25 mg of catalyst, with a 1 h reaction time. The resulting slurry was dropcast

onto the Si₃N₄ membrane of the cell to allow for intimate contact with the window while 19 μ L of the reaction liquor was charged in the static liquid reservoir to replicate solvent effects. Partial fluorescence yield spectra were acquired using a Vortex EM silicon drift detector.

X-ray Photoemission Spectroscopy. A commercial SPECS AP-XPS chamber equipped with a PHOIBOS 150 EP MCD-9 analyzer in the Chemistry Division of Brookhaven National Laboratory was used for XPS measurements. For energy calibration, the Ce 3d photoemission line with the strongest Ce⁴⁺ feature at 916.9 eV, was used. The powder catalysts were drop cast onto a roughened aluminum plate and then loaded into the AP-XPS chamber. All XPS measurements were conducted at room temperature under UHV conditions using an Al K α X-ray anode (1486.6 eV) where the pass energy was 50 eV and averaged over 15 scans with a dwell time of 0.1 s.

X-ray Absorption Spectroscopy (XAS). In situ XAS spectra were collected at the Inner Shell Spectroscopy beamline 8-ID at the National Synchrotron Light Source II in Brookhaven National Laboratory. The Pd K-edge was collected under in situ conditions using a custom-made high pressure flow reactor, shown in Figure S29 which was constructed from 316 stainless steel. XAS spectra were recorded in fluorescence mode using a PIPS detector. Pd foil was measured for energy calibration, using ion chambers, by moving the reaction cell out of the beam path. A CH₄ saturated flow of a 0.01 M solution of H₂O₂ with a rate of 0.1 mL/min was introduced to a custom-made reaction cell with a fixed catalyst bed placed in between two quartz wool plugs. The flow was controlled using a high-pressure compact pump (Azura, Knauer), the pressure in the reaction cell was maintained using a 34 bar back-pressure regulator (UpChurch) in addition to the use of graphite windows to withstand the cell pressure while accommodating the beam, while the tests were carried out at 50, 70, and 90 °C. To determine the redox properties of the materials prior to MtM reaction a H₂O solution saturated with CH₄ was introduced into the cell (34 bar, 50, 70, and 90 °C), denoted as simply CH₄ in the relevant figures.

In Situ ¹H Nuclear Magnetic Resonance (NMR). In situ ¹H NMR experiments were collected on a Bruker 700 MHz spectrometer, equipped with a z-shielded gradient triple resonance 5 mm TCI cryoprobe. Temperature calibration was achieved using ethylene glycol. Each transient spectrum was acquired with 64 scans and a relaxation delay of 2 s. The probe was preheated to the desired temperature (75 or 90 °C) before loading the high-pressure NMR tube (SP Industries Co., 524-PV-7, 5 mm O.D. and 7 in. length) into the spectrometer. The spectra acquisition commenced after temperature equilibration for ca. 13–14 min. The NMR tube was loaded with Pd-iC-CeO₂ (2.3 mg) and 0.5 M H₂O₂ in H₂O/D₂O solution (3% H₂O; 97% D₂O; 400 μ L), pressurized with 5 bar methane. The reaction constants were calculated by curve-fitting the time-resolved [MeOH] profile using pseudo-first-order rate equation: $[\text{MeOH}] = a \times \exp(-k \times t) + b$.

Density Functional Theory (DFT) Calculations. The calculations were performed using density functional theory (DFT) as implemented in VASP code (version 6.3.0),³⁵ which uses the slab-superficial approach.³⁶ The projector augmented wave (PAW) method³⁷ was used to describe the valence electrons of the atomic species: Ce (4f, 5s, 5p, 5d, 6s), O (2s, 2p), Pd(4p, 4d, 5s), C(2s, 2p) and H (1s), with a plane-wave cutoff energy of 415 eV. Electron localization due to electron transfer from the metal (or C species) to the oxide support, has been treated by means of the DFT + *U* approach proposed by Dudarev et al.,³⁸ with a *U*_{eff} value of *U* – *J* = 4.5 eV for the Ce 4f electrons. Additionally, the generalized gradient approximation (GGA), as suggested by Perdew, Burke, and Ernzerhof (PBE) was used.³⁹ Long-range dispersion corrections were considered with DFT lattice constants, employing the so-called DFT-D3 approach.^{40,41}

The CeO₂(111) surface with (3 × 3) periodicity was modeled with an optimized lattice constant of 5.485 Å for bulk CeO₂. All surface models used in this work have two O–Ce–O trilayers slabs and ~21 Å of vacuum separation between consecutive slabs. All atoms in the bottom O–Ce–O trilayer were kept fixed at their optimized bulk-

truncated positions during geometry optimization, whereas the rest of the atoms were allowed to fully relax. A $(2 \times 2 \times 1)$ k -point mesh, according to the Monkhorst–Pack method, is used to sample the Brillouin zone.^{41,42} To create the Pd-CeO₂ and Pd-iC-CeO₂ models, rhombohedral planar Pd₄ clusters were considered. In the case of Pd-CeO₂, this cluster is in direct contact with the ceria support, and the four Pd atoms collectively transfer one e⁻, resulting in the reduction of one Ce⁴⁺ ion to Ce³⁺ species (see Figure 5G). In contrast, the Pd-iC-CeO₂ model was created by inserting four (C–H) species below the rhombohedral Pd₄ structure forming Pd–C–O bonds. After the structure is optimized, it is observed that only one Pd atom forms a bond with the oxidic support (see Figure 5H) and that each of the four C atoms transfers one e⁻, leading to the formation of four Ce³⁺ species. Additionally, the Pd₄ nanostructure, similar to the Pd-CeO₂ case, donates another e⁻, forming a fifth Ce³⁺ species. The charge analysis involved calculating Bader charges on Pd and estimating the oxidation state of Ce atoms based on their local magnetic moment. This magnetic moment, representing the difference between up and down spin on the atoms, was obtained by integrating the site- and angular momentum projected spin-resolved density of states over spheres with radii chosen as the Wigner–Seitz radii of the PAW potentials. For reduced Ce ions, the occupation of Ce *f* states is close to 1, and the magnetic moment is ~ 1 μ B. Therefore, these ions are referred to as Ce³⁺. It is important to note that the inclusion of H-bonded C species prevents the formation of oxygen vacancies through the formation of CO species, which would result from the removal of lattice oxygen. For the gas-phase calculations of the CH₄, H₂O₂, and H₂O molecules, a $(15 \times 14 \times 13)$ Å³ cell was employed, with Γ -point only.

The (co)adsorption energies of methane, hydrogen peroxide, and the 8H₂O·2OH(aq) complex were calculated according to the following equation

$$E_{\text{ads}} = E[(m\text{CH}_4 + n\text{H}_2\text{O}_2 + l(8\text{H}_2\text{O}\cdot 2\text{OH}(\text{aq}))/\text{Pd}(-\text{iC})-\text{CeO}_2] - E[\text{Pd}(-\text{iC})-\text{CeO}_2] - mE[\text{CH}_4\text{gas}] - nE[\text{H}_2\text{O}_2\text{gas}] - lE[8\text{H}_2\text{O}\cdot 2\text{OH}(\text{aq})]$$

where $E[(m\text{CH}_4 + n\text{H}_2\text{O}_2 + l\text{H}_2\text{O})/\text{Pd}(-\text{iC})-\text{CeO}_2]$ is the total energy of m methane, n hydrogen peroxide and l water molecules (co)adsorbed on the surface with $n = 0, 1, m = 0-3, l = 0, 1$, $E[\text{Pd}(-\text{iC})-\text{CeO}_2]$ is the total energy of the clean model catalyst: Pd-CeO₂ or Pd-iC-CeO₂, $E[\text{CH}_4\text{gas}]$ and $E[\text{H}_2\text{O}_2\text{gas}]$ are the energies of the methane, hydrogen peroxide and water molecules in the gas phase. $E[8\text{H}_2\text{O}\cdot 2\text{OH}(\text{aq})]$ is the energy of the 8H₂O·2OH(aq) complex far from the surface.

To identify transition state (TS) structures, the climbing image nudged elastic band technique (CI-NEB) was used.⁴³ Among all the TSs discussed in this study, a sole imaginary frequency has been identified. Conducting complete geometry optimizations starting from the nearest configurations behind and ahead (along the reaction path) of this TS leads to a nondissociated state and a dissociated state, respectively. Within the computed potential energy profiles, the activation energy (E_{act}), defined as the difference between the energy of the transition state (ETS) and the initial state (EIS), serves as an indicator of the activation energy.

■ ASSOCIATED CONTENT

Data Availability Statement

The DFT data that support the findings of this study are available in Materials Cloud {<https://www.materialscloud.org/home>} with the identifier DOI: 10.24435/materialscloud:dz-zz. The data is also available from the authors upon reasonable request.

SI Supporting Information

The Supporting Information is available free of charge at <https://pubs.acs.org/doi/10.1021/jacs.4c04815>.

Experimental results: Detailed methane to methanol product distribution, characterization of the material (diffraction, XANES, XPS, ATR-IR, TGA, STEM-EELS), dispersion calculations, and schematics for high pressure gas–solid–liquid characterization cells. Theoretical results: Expanded discussion of the mechanism of methanol formation on Pd-CeO₂, hydrogen peroxide decomposition, charge density difference plots (CDDP) and density of states (PDOS) during the reaction, and additional justification of the Langmuir–Hinshelwood (PDF)

Eley–Rideal Pd-CeO₂ (MP4)

Eley–Rideal Pd-iC-CeO₂ (MP4)

■ AUTHOR INFORMATION

Corresponding Authors

Pablo G. Lustemberg – CSIC, Instituto de Catálisis y Petroleoquímica, 28049 Madrid, Spain; orcid.org/0000-0003-4058-4023; Email: p.lustemberg@csic.es

M. Verónica Ganduglia-Pirovano – CSIC, Instituto de Catálisis y Petroleoquímica, 28049 Madrid, Spain; orcid.org/0000-0003-2408-8898; Email: vgp@icp.csic.es

Sanjaya D. Senanayake – Chemistry Division, Brookhaven National Laboratory, Upton, New York 11973, United States; orcid.org/0000-0003-3991-4232; Email: ssenanay@bnl.gov

Authors

Juan D. Jiménez – Chemistry Division, Brookhaven National Laboratory, Upton, New York 11973, United States; orcid.org/0000-0003-4710-1047

Maila Danielis – Polytechnic Department, University of Udine and INSTM, 33100 Udine, Italy; orcid.org/0000-0001-8469-9282

Estefanía Fernández-Villanueva – CSIC, Instituto de Catálisis y Petroleoquímica, 28049 Madrid, Spain; Universitat Politècnica de València, 46022 Valencia, Spain; orcid.org/0000-0002-9419-0786

Sooyeon Hwang – Center for Functional Nanomaterials, Brookhaven National Laboratory, Upton, New York 11973, United States; orcid.org/0000-0001-5606-6728

Iradwikanari Waluyo – National Synchrotron Light Source II, Brookhaven National Laboratory, Upton, New York 11973, United States; orcid.org/0000-0002-4046-9722

Adrian Hunt – National Synchrotron Light Source II, Brookhaven National Laboratory, Upton, New York 11973, United States; orcid.org/0000-0002-5283-9647

Dominik Wierzbicki – National Synchrotron Light Source II, Brookhaven National Laboratory, Upton, New York 11973, United States

Jie Zhang – Ames National Laboratory, Iowa State University, Ames, Iowa 50011, United States

Long Qi – Ames National Laboratory, Iowa State University, Ames, Iowa 50011, United States

Alessandro Trovarelli – Polytechnic Department, University of Udine and INSTM, 33100 Udine, Italy; orcid.org/0000-0002-1396-4031

José A. Rodríguez – Chemistry Division, Brookhaven National Laboratory, Upton, New York 11973, United States; Department of Chemistry, State University of New York Stony Brook, Stony Brook, New York 11794, United States; orcid.org/0000-0002-5680-4214

Sara Colussi – Polytechnic Department, University of Udine and INSTM, 33100 Udine, Italy; orcid.org/0000-0001-5316-1746

Complete contact information is available at:
<https://pubs.acs.org/10.1021/jacs.4c04815>

Notes

The authors declare no competing financial interest.

ACKNOWLEDGMENTS

Work carried out at Brookhaven National Laboratory (BNL) was supported by the U.S. Department of Energy (DOE), Office of Science, Office of Basic Energy Sciences, Chemical Sciences, Geosciences, and Biosciences (GSGB) Division, Catalysis Science Program under contract no. DE-SC0012704. J.D.J. acknowledges support from the BNL Goldhaber Distinguished Fellowship. M.D. and S.C. acknowledge the Fondazione CRUI for funding under “Go for IT” Program (CUP G29C20000830001). E.F.V. thanks UPV for her Margarita Salas postdoctoral fellowship and both Spanish MIU and European Union-Next generation EU for financial support. M.V.G.P. and P.G.L. acknowledge support under Grant PID2021-128915NB-I00 funded by MCIN/AEI/10.13039/501100011033/ and by ERDF, UE. This research used resources of the 23-ID-2 (IOS) and 8-ID beamlines of the National Synchrotron Light Source II, a DOE Office of Science User Facility operated by BNL under Contract No. DE-SC0012704. This research used the Electron Microscopy facility of the Center for Functional Nanomaterials (CFN), a DOE Office of Science User Facility also operated by BNL under Contract No. DE-SC0012704. L.Q. and J.Z. were supported by the DOE, Office of Science, Office of Basic Energy Sciences, CSGB Division, Catalysis Science program. Ames National Laboratory is operated for the DOE by Iowa State University under Contract No. DEAC02-07CH11358. J.Z. and L.Q. thank Donald B. Fulton and Jeffrey A. Purslow for their assistance in setting up the in situ NMR experiments. Computer time provided by the RES (Red Española de Supercomputación) resources at MareNostrum 4 (BSC, Barcelona) node and by Centro de Computación Científica-Universidad Autónoma de Madrid (CCC-UAM) is acknowledged. This research project was also made possible through the access granted by the Galician Supercomputing Center (CESGA) to its supercomputing infrastructure. The supercomputer FinisTerae III and its permanent data storage system have been funded by the Spanish Ministry of Science and Innovation, the Galician Government, and the European Regional Development Fund (ERDF).

REFERENCES

- (1) Shaw, W. J.; Kidder, M. K.; Bare, S. R.; Delferro, M.; Morris, J. R.; Toma, F. M.; Senanayake, S. D.; Autrey, T.; Biddinger, E. J.; Boettcher, S.; et al. A US perspective on closing the carbon cycle to defossilize difficult-to-electrify segments of our economy. *Nat. Rev. Chem.* **2024**, *8* (5), 376–400.
- (2) Baek, J.; Rungtaweeworanit, B.; Pei, X.; Park, M.; Fakra, S. C.; Liu, Y.-S.; Matheu, R.; Alshimmiri, S. A.; Alshehri, S.; Trickett, C. A.; et al. Bioinspired Metal–Organic Framework Catalysts for Selective Methane Oxidation to Methanol. *J. Am. Chem. Soc.* **2018**, *140* (51), 18208–18216.
- (3) Sushkevich, V. L.; Palagin, D.; Ranocchiari, M.; van Bokhoven, J. A. Selective anaerobic oxidation of methane enables direct synthesis of methanol. *Science* **2017**, *356* (6337), 523–527.
- (4) Ravi, M.; Sushkevich, V. L.; Knorpp, A. J.; Newton, M. A.; Palagin, D.;

Pinar, A. B.; Ranocchiari, M.; van Bokhoven, J. A. Misconceptions and challenges in methane-to-methanol over transition-metal-exchanged zeolites. *Nat. Catal.* **2019**, *2* (6), 485–494.

(3) Kwon, Y.; Kim, T. Y.; Kwon, G.; Yi, J.; Lee, H. Selective Activation of Methane on Single-Atom Catalyst of Rhodium Dispersed on Zirconia for Direct Conversion. *J. Am. Chem. Soc.* **2017**, *139* (48), 17694–17699.

(4) Wu, X.; Zhang, Q.; Li, W.; Qiao, B.; Ma, D.; Wang, S. L. Atomic-scale Pd on 2D titania sheets for selective oxidation of methane to methanol. *ACS Catal.* **2021**, *11* (22), 14038–14046.

(5) Lustemberg, P. G.; Palomino, R. M.; Gutiérrez, R. A.; Grinter, D. C.; Vorokhta, M.; Liu, Z.; Ramírez, P. J.; Matolín, V.; Ganduglia-Pirovano, M. V.; Senanayake, S. D.; Rodríguez, J. A. Direct Conversion of Methane to Methanol on Ni-Ceria Surfaces: Metal–Support Interactions and Water-Enabled Catalytic Conversion by Site Blocking. *J. Am. Chem. Soc.* **2018**, *140* (24), 7681–7687.

(6) Liu, Z.; Huang, E.; Orozco, L.; Liao, W.; Palomino, R. M.; Rui, N.; Duchoň, T.; Nemsák, S.; Grinter, D. C.; Mahapatra, M.; et al. Water-promoted interfacial pathways in methane oxidation to methanol on a CeO₂-Cu₂O catalyst. *Science* **2020**, *368* (6490), 513–517.

(7) Liang, Z.; Li, T.; Kim, M.; Asthagiri, A.; Weaver, J. F. Low-temperature activation of methane on the IrO₂ (110) surface. *Science* **2017**, *356* (6335), 299–303.- (8) Senanayake, S. D.; Rodríguez, J. A.; Weaver, J. F. Low Temperature Activation of Methane on Metal-Oxides and Complex Interfaces: Insights from Surface Science. *Acc. Chem. Res.* **2020**, *53* (8), 1488–1497.

(8) Li, M.; Shan, J.; Giannakakis, G.; Ouyang, M.; Cao, S.; Lee, S.; Allard, L. F.; Flytzani-Stephanopoulos, M. Single-step Selective Oxidation of Methane to Methanol in the Aqueous Phase on Iridium-based Catalysts. *Appl. Catal., B* **2021**, *292*, No. 120124.

(9) Xie, J.; Jin, R.; Li, A.; Bi, Y.; Ruan, Q.; Deng, Y.; Zhang, Y.; Yao, S.; Sankar, G.; Ma, D.; Tang, J. Highly selective oxidation of methane to methanol at ambient conditions by titanium dioxide-supported iron species. *Nat. Catal.* **2018**, *1* (11), 889–896.

(10) Farmer, J. A.; Campbell, C. T. Ceria Maintains Smaller Metal Catalyst Particles by Strong Metal-Support Bonding. *Science* **2010**, *329* (5994), 933–936 accessed 2024/01/08.

(11) Tomkins, P.; Ranocchiari, M.; van Bokhoven, J. A. Direct conversion of methane to methanol under mild conditions over Cu-zeolites and beyond. *Acc. Chem. Res.* **2017**, *50* (2), 418–425.

(12) Li, H.; Shen, Y.; Xiao, X.; Jiang, H.; Gu, Q.; Zhang, Y.; Lin, L.; Luo, W.; Zhou, S.; Zhao, J.; et al. Controlled-Release Mechanism Regulates Rhodium Migration and Size Redistribution Boosting Catalytic Methane Conversion. *ACS Catal.* **2023**, *13* (2), 1197–1206.

(13) Rahim, M. H. A.; Forde, M. M.; Jenkins, R. L.; Hammond, C.; He, Q.; Dimitratos, N.; Lopez-Sanchez, J. A.; Carley, A. F.; Taylor, S. H.; Willock, D. J.; et al. Oxidation of methane to methanol with hydrogen peroxide using supported gold–palladium alloy nanoparticles. *Angew. Chem., Int. Ed.* **2013**, *52* (4), 1280–1284.

(14) Jin, Z.; Wang, L.; Zuidema, E.; Mondal, K.; Zhang, M.; Zhang, J.; Wang, C.; Meng, X.; Yang, H.; Mesters, C.; Xiao, F. S. Hydrophobic zeolite modification for in situ peroxide formation in methane oxidation to methanol. *Science* **2020**, *367* (6474), 193–197.

(15) Shan, J.; Li, M.; Allard, L. F.; Lee, S.; Flytzani-Stephanopoulos, M. Mild oxidation of methane to methanol or acetic acid on supported isolated rhodium catalysts. *Nature* **2017**, *551* (7682), 605–608.

(16) Agarwal, N.; Freakley, S. J.; McVicker, R. U.; Althahban, S. M.; Dimitratos, N.; He, Q.; Morgan, D. J.; Jenkins, R. L.; Willock, D. J.; Taylor, S. H.; et al. Aqueous Au-Pd colloids catalyze selective CH₄ oxidation to CH₃OH with O₂ under mild conditions. *Science* **2017**, *358* (6360), 223–227.

(17) Szécsényi, A.; Li, G.; Gascon, J.; Pidko, E. A. Mechanistic Complexity of Methane Oxidation with H₂O₂ by Single-Site Fe/ZSM-5 Catalyst. *ACS Catal.* **2018**, *8* (9), 7961–7972.

(18) Yu, B.; Cheng, L.; Dai, S.; Jiang, Y.; Yang, B.; Li, H.; Zhao, Y.; Xu, J.; Zhang, Y.; Pan, C.; et al. Silver and Copper Dual Single Atoms

Boosting Direct Oxidation of Methane to Methanol via Synergistic Catalysis. *Adv. Sci.* **2023**, *10* (26), No. 2302143.

(19) Lou, Y.; Jiang, F.; Zhu, W.; Wang, L.; Yao, T.; Wang, S.; Yang, B.; Yang, B.; Zhu, Y.; Liu, X. CeO₂ supported Pd dimers boosting CO₂ hydrogenation to ethanol. *Appl. Catal., B* **2021**, *291*, No. 120122.

(20) Cao, J.; Lewis, R. J.; Qi, G.; Bethell, D.; Howard, M. J.; Harrison, B.; Yao, B.; He, Q.; Morgan, D. J.; Ni, F.; et al. Methane Conversion to Methanol Using Au/ZSM-5 is Promoted by Carbon. *ACS Catal.* **2023**, *13* (11), 7199–7209.

(21) Jiménez, J. D.; Betancourt, L. E.; Danielis, M.; Zhang, H.; Zhang, F.; Orozco, I.; Xu, W.; Llorca, J.; Liu, P.; Trovarelli, A.; et al. Identification of Highly Selective Surface Pathways for Methane Dry Reforming Using Mechanochemical Synthesis of Pd–CeO₂. *ACS Catal.* **2022**, *12* (20), 12809–12822.

(22) Danielis, M.; Colussi, S.; de Leitenburg, C.; Soler, L.; Llorca, J.; Trovarelli, A. Outstanding Methane Oxidation Performance of Palladium-Embedded Ceria Catalysts Prepared by a One-Step Dry Ball-Milling Method. *Angew. Chem., Int. Ed.* **2018**, *57* (32), 10212–10216.

(23) Danielis, M.; Jiménez, J. D.; Rui, N.; Moncada, J.; Betancourt, L. E.; Trovarelli, A.; Rodriguez, J. A.; Senanayake, S. D.; Colussi, S. Tuning the hydrogenation of CO₂ to CH₄ over mechano-chemically prepared palladium supported on ceria. *Appl. Catal., A* **2023**, *660*, No. 119185.

(24) Ravi, M.; Ranocchiari, M.; van Bokhoven, J. A. The Direct Catalytic Oxidation of Methane to Methanol—A Critical Assessment. *Angew. Chem., Int. Ed.* **2017**, *56* (52), 16464–16483.

(25) Rahim, M. H. A.; Armstrong, R. D.; Hammond, C.; Diimitratos, N.; Freakley, S. J.; Forde, M. M.; Morgan, D. J.; Lalev, G.; Jenkins, R. L.; Lopez-Sanchez, J. A.; et al. Low temperature selective oxidation of methane to methanol using titania supported gold palladium copper catalysts. *Catal. Sci. Technol.* **2016**, *6* (10), 3410–3418. Sushkevich, V. L.; van Bokhoven, J. A. Methane-to-Methanol: Activity Descriptors in Copper-Exchanged Zeolites for the Rational Design of Materials. *ACS Catal.* **2019**, *9* (7), 6293–6304.

(26) Zhang, Z.; Tian, J.; Lu, Y.; Yang, S.; Jiang, D.; Huang, W.; Li, Y.; Hong, J.; Hoffman, A. S.; Bare, S. R.; et al. Memory-dictated dynamics of single-atom Pt on CeO₂ for CO oxidation. *Nat. Commun.* **2023**, *14* (1), No. 2664.

(27) McVicker, R.; Agarwal, N.; Freakley, S. J.; He, Q.; Althabban, S.; Taylor, S. H.; Kiely, C. J.; Hutchings, G. J. Low temperature selective oxidation of methane using gold-palladium colloids. *Catal. Today* **2020**, *342*, 32–38. Gao, F.; Goodman, D. W. Pd–Au bimetallic catalysts: understanding alloy effects from planar models and (supported) nanoparticles. *Chem. Soc. Rev.* **2012**, *41* (24), 8009–8020.

(28) Carter, J. H.; Lewis, R. J.; Demetriou, N.; Williams, C.; Davies, T. E.; Qin, T.; Dummer, N. F.; Morgan, D. J.; Willock, D. J.; Liu, X.; et al. The selective oxidation of methane to methanol using in situ generated H₂O₂ over palladium-based bimetallic catalysts. *Catal. Sci. Technol.* **2023**, *13* (20), 5848–5858.

(29) Lear, T.; Marshall, R.; Antonio Lopez-Sanchez, J.; Jackson, S. D.; Klapötke, T. M.; Bäumer, M.; Rupprechter, G.; Freund, H.-J.; Lennon, D. The application of infrared spectroscopy to probe the surface morphology of alumina-supported palladium catalysts. *J. Chem. Phys.* **2005**, *123* (17), No. 174706. Jbir, I.; Couble, J.; Khaddar-Zine, S.; Ksibi, Z.; Meunier, F.; Bianchi, D. Individual heat of adsorption of adsorbed CO species on palladium and Pd–Sn nanoparticles supported on Al₂O₃ by using temperature-programmed adsorption equilibrium methods. *ACS Catal.* **2016**, *6* (4), 2545–2558.

(30) Ebbesen, S. D.; Mojet, B. L.; Lefferts, L. The influence of water and pH on adsorption and oxidation of CO on Pd/Al₂O₃—an investigation by attenuated total reflection infrared spectroscopy. *Phys. Chem. Chem. Phys.* **2009**, *11* (4), 641–649.

(31) Li, Y.; Fu, Q.; Flytzani-Stephanopoulos, M. Low-temperature water-gas shift reaction over Cu- and Ni-loaded cerium oxide catalysts. *Appl. Catal., B* **2000**, *27* (3), 179–191.

(32) Engdahl, A.; Nelander, B. The HOOH–HOO complex. A matrix isolation study. *Phys. Chem. Chem. Phys.* **2004**, *6* (4), 730–734.

(33) Bai, S.; Liu, F.; Huang, B.; Li, F.; Lin, H.; Wu, T.; Sun, M.; Wu, J.; Shao, Q.; Xu, Y.; Huang, X. High-efficiency direct methane conversion to oxygenates on a cerium dioxide nanowires supported rhodium single-atom catalyst. *Nat. Commun.* **2020**, *11* (1), No. 954.

(34) Wang, W.-C.; Chen, S.-Y.; Glans, P.-A.; Guo, J.; Chen, R.-J.; Fong, K.-W.; Chen, C.-L.; Gloter, A.; Chang, C.-L.; Chan, T.-S.; et al. Towards understanding the electronic structure of Fe-doped CeO₂ nanoparticles with X-ray spectroscopy. *Phys. Chem. Chem. Phys.* **2013**, *15* (35), 14701–14707.

(35) Kresse, G.; Hafner, J. Ab initio molecular dynamics for liquid metals. *Phys. Rev. B* **1993**, *47* (1), No. 558. Kresse, G.; Hafner, J. Ab initio molecular-dynamics simulation of the liquid-metal–amorphous-semiconductor transition in germanium. *Phys. Rev. B* **1994**, *49* (20), No. 14251. Kresse, G.; Furthmüller, J. Efficient iterative schemes for ab initio total-energy calculations using a plane-wave basis set. *Phys. Rev. B* **1996**, *54* (16), No. 11169. Kresse, G.; Furthmüller, J. Efficiency of ab-initio total energy calculations for metals and semiconductors using a plane-wave basis set. *Comput. Mater. Sci.* **1996**, *6* (1), 15–50. Kresse, G.; Joubert, D. From ultrasoft pseudopotentials to the projector augmented-wave method. *Phys. Rev. B* **1999**, *59* (3), No. 1758.

(36) Payne, M. C.; Teter, M. P.; Allan, D. C.; Arias, T.; Joannopoulos, A. J. Iterative minimization techniques for ab initio total-energy calculations: molecular dynamics and conjugate gradients. *Rev. Mod. Phys.* **1992**, *64* (4), No. 1045.

(37) Blöchl, P. E. Projector augmented-wave method. *Phys. Rev. B* **1994**, *50* (24), No. 17953.

(38) Dudarev, S. L.; Botton, G. A.; Savrasov, S. Y.; Humphreys, C.; Sutton, A. P. Electron-energy-loss spectra and the structural stability of nickel oxide: An LSDA+ U study. *Phys. Rev. B* **1998**, *57* (3), No. 1505.

(39) Perdew, J. P.; Burke, K.; Ernzerhof, M. Generalized gradient approximation made simple. *Phys. Rev. Lett.* **1996**, *77* (18), No. 3865.

(40) Grimme, S.; Antony, J.; Ehrlich, S.; Krieg, H. A consistent and accurate ab initio parametrization of density functional dispersion correction (DFT-D) for the 94 elements H–Pu. *J. Chem. Phys.* **2010**, *132* (15), No. 154104, DOI: 10.1063/1.3382344.

(41) Grimme, S.; Ehrlich, S.; Goerigk, L. Effect of the damping function in dispersion corrected density functional theory. *J. Comput. Chem.* **2011**, *32* (7), 1456–1465.

(42) Monkhorst, H. J.; Pack, J. D. Special points for Brillouin-zone integrations. *Phys. Rev. B* **1976**, *13* (12), No. 5188.

(43) Henkelman, G.; Uberuaga, B. P.; Jónsson, H. A climbing image nudged elastic band method for finding saddle points and minimum energy paths. *J. Chem. Phys.* **2000**, *113* (22), 9901–9904.